AIAA Atmospheric Flight Mechanics 2010 Conference **2010-7938**
2-5 Aug 2010, Toronto, Ontario, Canada

Modeling Propeller Aerodynamics and Slipstream Effects on Small UAVs in Realtime

Michael S. Selig*
University of Illinois at Urbana-Champaign, Urbana, IL 61801, USA

This paper focuses on strong propeller effects in a full six degree-of-freedom (6-DOF) aerodynamic modeling of small UAVs at high angles of attack and high sideslip in maneuvers performed using large control surfaces at large deflections for aircraft with high thrust-to-weight ratios. For such configurations, the flight dynamics can be dominated by relatively large propeller forces and strong propeller slipstream effects on the downstream surfaces, e.g., wing, fuselage and tail. Specifically, the propeller slipstream effects include propeller wash flow speed effects, propeller wash lag in speed and direction, flow shadow effects and several more that are key to capturing flight dynamics behaviors that are observed to be common to high thrust-to-weight ratio aircraft. The overall method relies on a component-based approach, which is discussed in a companion paper, and forms the foundation of the aerodynamics model used in the RC flight simulator FS One. Piloted flight simulation results for a small RC/UAV configuration having a wingspan of 1765 mm (69.5 in) are presented here to highlight results of the high-angle propeller/aircraft aerodynamics modeling approach. Maneuvers simulated include knife-edge power-on spins, upright power-on spins, inverted power-on pirouettes, hovering maneuvers, and rapid pitch maneuvers all assisted by strong propeller-force and propeller-wash effects. For each case, the flight trajectory is presented together with time histories of aircraft state data during the maneuvers, which are discussed.

Nomenclature

A	=	propeller disc area
a	=	airfoil lift curve slope (2π)
C_Q	=	propeller torque coefficient ($Q/\rho n^2 D^5$)
C_T	=	propeller thrust coefficient ($T/\rho n^2 D^4$)
D	=	propeller diameter
I	=	mass moment of inertia
J	=	propeller advance ratio based on V_N
k	=	constant, semi-empirical correction coefficient
M	=	pitching moment about y-axis (positive nose up)
m	=	jet flow parameter ($V_{\infty N}/V_{\text{disc},N}$)
m_j	=	mass flow rate
N	=	yawing moment about z-axis (positive nose right)
n	=	propeller rotational speed (revs/sec)
N_j	=	propeller normal force due to angle of attack (method 2)
N_P	=	propeller yawing moment due to angle of attack
p, q, r	=	body-axis roll, pitch and yaw rate

*Associate Professor, Department of Aerospace Engineering, 104 S. Wright St. Senior Member AIAA. http://www.ae.illinois.edu/m-selig

P_N	=	propeller normal force due to angle of attack (method 1)
Q	=	propeller axial torque
R	=	propeller radius
T	=	propeller axial thrust
V	=	flow velocity
w	=	propeller induced velocity
w_0	=	propeller induced velocity at hover, reference speed
X, Y, Z	=	inertial coordinates
x, y, z	=	body-axis coordinates, $+x$ out nose, $+y$ out right wing, $+z$ down
RPM	=	propeller rotational speed (revs/min)
TED	=	trailing edge down
TEL	=	trailing edge left
TEU	=	trailing edge up

Subscripts

N	=	normal component
R	=	relative component

Symbols

α	=	angle of attack ($\arctan(w/u)$)
β	=	sideslip angle ($\arcsin(v/V)$)
δ_a	=	aileron deflection $[(\delta_{a,r} - \delta_{a,l})/2]$, right +TEU, left +TEU
δ_e	=	elevator deflection, +TED
δ_r	=	rudder deflection, +TEL
η_s	=	dynamic pressure ratio for flow shadow (shielding) effect
Ω	=	propeller rotational speed (rad/sec)
ϕ, θ, ψ	=	bank angle, pitch angle, heading angle
ρ	=	air density
σ	=	propeller solidity (blade area/disc area)

I. Introduction

Over the past 20 yrs, advances in propeller-driven propulsion and light-weight materials and electronics have led to current-day RC/UAV fixed-wing aircraft configurations with thrust-to-weight ratios of nearly 2:1. This level of performance combined with large control surfaces and lifting surfaces immersed in high-speed propeller wash has produced a "new breed" of ultra-agile aircraft that can be flown over an envelope that ranges from conventional fixed-wing cruise flight to a stop-and-stare hover attitude, and nearly anything aerobatic in between. This extreme performance presents new challenges in propeller/airframe modeling and simulation.

Methods for modeling propeller aerodynamics in cruise flight are well known and literature on the subject abounds, e.g., see Ref. 1. Challenges exist, however, in modeling the transition from level cruise flight to hover, including unsteady effects. More generally, propeller aerodynamics at any flight condition, that is, any aircraft attitude and speed, must be addressed to capture full-envelope flight dynamics, which can occur in upsets or ultra-agile/aerobatic maneuvers. Also, propeller modeling must include direct propeller forces and moments as well as propeller wash effects on downstream surfaces and vice versa. Finally, all of these effects must be combined in a "seamless" and computationally-efficient methodology when applied in a realtime piloted simulation environment.

This paper discusses an approach to modeling propeller aerodynamics covering the aforementioned range of issues for application in a realtime full-envelope simulation environment for ultra-agile RC/UAV configurations. The propeller methodology described here is included as one element of a larger full-envelope simulation framework that is discussed in a companion paper.[2] As such, some overlap between the two papers exists.

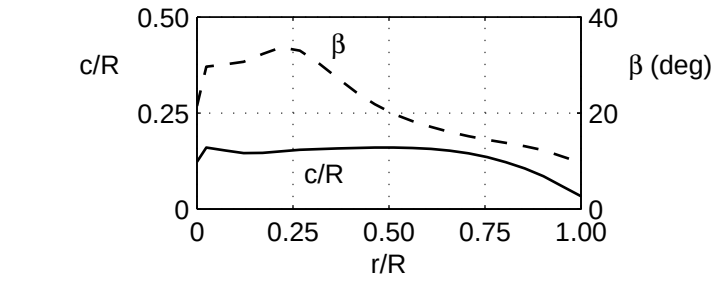

Front View

Side View

Figure 1. APC Sport 14×8 geometric characteristics and photographic projections.

II. Propeller Forces and Moments

For the normal working state (steady axial-flow conditions), the propeller thrust and torque are given by

$$T = \rho n^2 D^4 C_T \tag{1}$$

$$Q = \rho n^2 D^5 C_Q \tag{2}$$

where the thrust and torque coefficients are determined through lookup tables on the advance ratio given by

$$J = \frac{V_N}{n\,D} \tag{3}$$

where V_N is the normal component of the relative flow at the propeller disc. The propeller thrust and torque coefficients (Eqs. 1 and 2) are determined from blade element momentum theory, in particular, using the code PROPID.[3–5] For this analysis, the propeller chord and twist distributions are determined from digitized photographic projections of the top and side views as shown in Fig. 1. These data together with corresponding propeller airfoil data are used to determine the resulting coefficient C_T and C_Q data. Figure 2 shows these predictions for the propeller shown in Fig. 1.

Apart from the basic propeller aerodynamics expressed in Eqs. 1 and 2, a number of other factors must be considered for any general motion and propeller attitude. These include propeller normal force P_N and P-factor (yawing moment) N_P when the flow is not axial, i.e. when the propeller is at an angle of attack to the flow. These effects are given by[1]

$$P_N = \frac{\sigma q A}{2}\left\{\overline{C}_l + \frac{aJ}{2\pi}\ln\left[1+\left(\frac{\pi}{J}\right)^2\right] + \frac{\pi}{J}C_d\right\}\alpha \tag{4}$$

$$N_P = \frac{-\sigma q A R}{2}\left\{\frac{2\pi}{3J}\overline{C}_l + \frac{a}{2}\left[1-\left(\frac{J}{\pi}\right)^2\ln\left(1+\left[\frac{\pi}{J}\right]^2\right)\right] - \frac{\pi}{J}C_d\right\}\alpha \tag{5}$$

where the average lift coefficient $\overline{C}_l$ is expressed as

$$\overline{C}_l = \left(\frac{3J}{2\pi}\right)\left[\frac{2}{\sigma q A}\frac{J}{\pi}T + C_d\right] \tag{6}$$

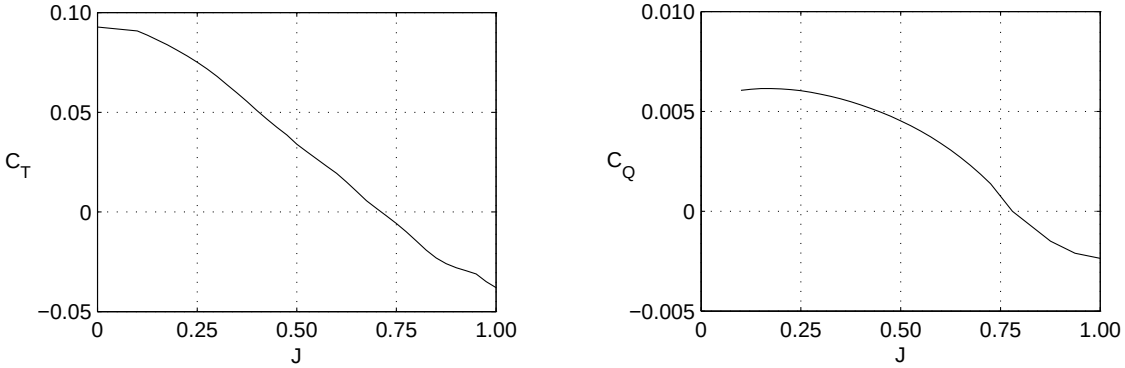

Figure 2. APC Sport 14×8 predicted thrust and torque characteristics.

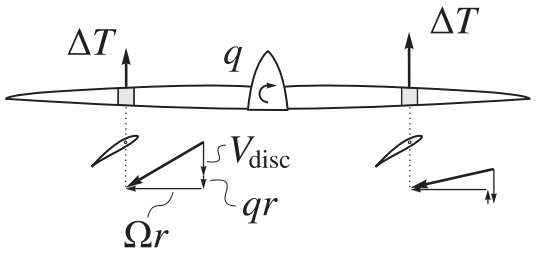

Figure 3. Illustration of propeller pitch damping effect due to differential local blade section angle of attack resulting from aircraft pitch rate.

Additional propeller moments are produced by the propeller angular accelerations as well as gyroscopic effects resulting from aircraft pitch and yaw rates, namely

$$Q_{\text{accel}} = I_{\text{prop}}\ddot{\Omega} \tag{7}$$

and

$$M_{\text{gyro}} = -I_{\text{prop}}\ddot{\Omega}\, r \tag{8}$$

$$N_{\text{gyro}} = I_{\text{prop}}\ddot{\Omega}\, q \tag{9}$$

where Ω is the propeller speed and positive for a right-handed propeller.

Another important effect is pitch and yaw damping moment produced by the propeller when rotated about the pitch and yaw axes, respectively. This damping arises from a difference in lift on one side of the disc vs the other due to an increase in local section angle of attack. Figure 3 depicts conceptually the case that produces a pitch damping moment due to pitch rate q (for clarity, swirl has been omitted from this drawing). The resulting moment is given by

$$M = k_d \frac{\rho}{2}\Omega^2 R^5 \arctan\left(\frac{q}{\Omega}\right) \tag{10}$$

$$N = k_d \frac{\rho}{2}\Omega^2 R^5 \arctan\left(\frac{r}{\Omega}\right) \tag{11}$$

where the parameter k can be approximated as

$$k_d \approx (2\pi)\pi\sigma \tag{12}$$

A second contribution to motion damping, particularly in conditions around hover, results from the propeller normal force. The propeller normal force given by Eq. 4 cannot be reliably applied when flying

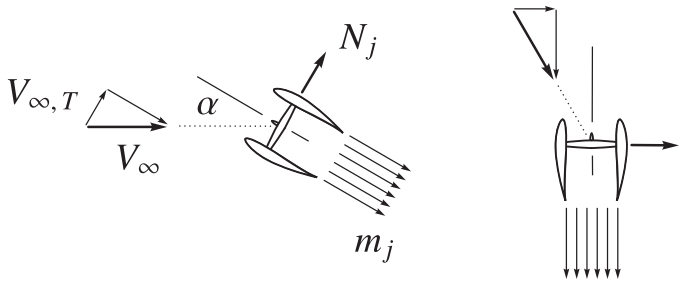

Figure 4. Normal force oriented for a jet flow (left) and ducted fan flow (right) along with key parameters defining the magnitude of the force.

in a near hover condition, and thus in the method that normal force is "washed out" in high angle flight. However, there is still a significant propeller normal force when maneuvering near hover. The effect is most easily explained by considering jet flow at an angle to the freestream or a ducted-fan arrangement in hover. Both are shown in Fig. 4 and represent the identical aerodynamic effect. For a jet engine in flight the normal force contributes to the lift; whereas, for a hovering ducted-fan vehicle the normal force contributes to the side force. And in the latter case, this side force represents a damping force (or drag) and thus detrimental to forward flight of a ducted fan; however, for an airplane in hover the damping force makes hovering flight less demanding of the pilot.

The normal force N_j for the ducted-jet arrangements shown in Fig. 4 is given by

$$N_j = m_j V_\infty \sin\alpha \tag{13}$$

$$= m_j V_{\infty,T} \tag{14}$$

This jet normal force[6] has also been called "ram drag" and "momentum drag" in the V/STOL literature, e.g., see Ref. 7. For a propeller, the slipstream flow is not turned as efficiently as that for ducted fan, and consequently the normal force is some fraction of that for jet/duct flows. This reduction in turning efficiency has been determined empirically to be in the range of 80% for propeller flows around smooth streamline fuselage cowlings and nearly 100% for cruciform-nose profile aerobatic foam aircraft in hover-type flying conditions (see Fig. 1 in companion paper[2]). Moreover, the effect is greatest when maneuvering around hovering flight. Thus, in the current approach this normal force is taken as

$$N_j = k_j(\rho A w_0) V_{\infty,T} \tag{15}$$

where w_0 is the induced velocity through the propeller disc and taken as that value for hover, that is

$$w_0 = \sqrt{\frac{T}{2\rho A}} \tag{16}$$

The resulting normal force is resolved into y and z components in the body axis and these forces damp translational motion. Also, this normal force at the plane of the propeller disc produces damping moments in pitch and yaw. Finally, to avoid counting the propeller normal force twice, this effect is "washed out" away from flight in hover conditions. Thus, the traditional propeller normal force (Eq. 4) and this jet effect (Eq. 15) both contribute to the normal force as a weighted sum not exceeding the maximum of either one.

Finally, all propeller forces and moments are resolved about the aircraft reference point in the body-axis coordinate system taking into account thrustline and position offsets.

III. Propeller Wake Flow Modeling

The development of a model of the slipstream is key to predicting the forces and moments on the downstream surfaces and hence aircraft motion. These downstream surfaces immersed in the propeller wake include, for example, the fuselage, wing root regions, and tail surfaces for a conventional configuration such

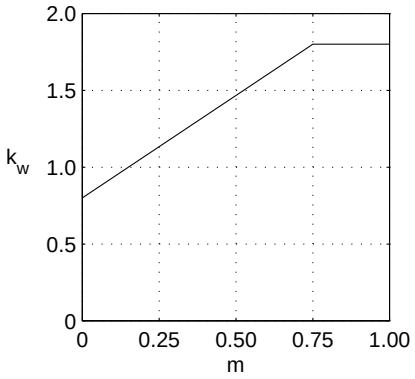

Figure 5. Induced velocity scale factor over the jet flow parameter range from 0 to 1.

as that considered in this paper. Many factors must be taken into account including wake size, axial speed, swirl, flow angle, curvature, lag (unsteady) effects and surface-propeller interactions as functions of propeller thrust, aircraft speed and orientation to the relative flow.

As a first step, flight in the full-envelope environment of an aerobatic ultra-agile RC/UAV ranges from hover (or static thrust conditions) to cruise flight. Moreover, flight in the vortex ring state (steep descent) and the windmill brake state are often encountered in aerobatic flight.

In static hover conditions, the wake of a propeller is similar to a free jet, and thus jet theory is applied here in developing a model for propeller wake flow in static conditions. For a jet, while the centerline jet speed does decay downstream, it occurs only after several jet diameters.[8–10] Assuming the propeller disc diameter to be equivalent to the jet exit diameter leads to the conclusion that the downstream flow speed at the tail on the centerline is nearly the same as that at the propeller disc, i.e. the propeller induced velocity in hover (Eq. 16). For the normal working state (e.g., the cruise flight conditions), the contraction of the propeller slipstream typically occurs within a few propeller diameters downstream at which point the downstream induced velocity is twice that at the disc.[11]

Based on the behavior of the downstream wake speed as described, the basic model for the induced velocity is given by

$$w_{\text{downstream}} = k_w w \tag{17}$$

where

$$k_w = \begin{cases} k_s & m < m_s \\ k_s + (m - m_s)(k_f - k_s)/(m_f - m_s) & m_f > m > m_s \\ k_f & m > m_f \end{cases} \tag{18}$$

and

$$m = \frac{V_{\infty N}}{V_{\text{disc},N}} \tag{19}$$

and from theory

$$w = \frac{1}{2}\left[-V_\infty + \sqrt{V_\infty^2 + \left(\frac{2T}{\rho A}\right)}\right] \tag{20}$$

Figure 5 graphically depicts Eq. 18 which is linear and increasing between the hover case (slow speed, "s") and near cruise condition (fast speed, "f") with typical values for the related constants. While reference is given here "slow" and "fast," these conditions might be better described respectively as a highly loaded propeller case (m near zero) and a lightly loaded case (m increasing) for a given speed V_∞. As shown in Fig. 5, away from hover (increasing m) the value for k_s approaches but does not reach 2. While a value of 2 is the ideal case for an isolated propeller, propeller-fuselage interaction effects reduce the downstream flow from that of the theoretical limit.

In addition to this dependence on the jet flow parameter m, the induced flow factor k_w is decayed as a function of the local flow angle at the respective component (e.g., wing root, fuselage panel, right horizontal

tail surface). Moreover this flow-angle decay envelope itself is a function of the jet parameter m. For the hover case, this wake flow angle is relatively wide (allowing for relatively wide excursions), while in the normal working state the wake is properly termed a slipstream and is relatively narrow. In the current approach this angle that determines the amount of decay (or no decay) is termed the "wake expansion angle," increasing as m approaches the hover state. An additional correction takes into account curved flight that results in curved wake/slipstream flow, affecting the local flow angle on the surface at which the propeller wash speed is being determined. Another angle correction applies as a result of the fanning out of the turbulent wake for low m (near 0) relative to high m (near 1).

Finally, the wake flow speed is lagged on downstream surfaces as a function of the wake flow speed at the disc. Thus, a throttle burst resulting in a rapid increase in flow at the disc will not be "felt" by a downstream surface until a short time later. In the method, first-order lags are used with a lag time constant that is a function of the propeller disc speed and distance between the propeller and each respective downstream surface.

The models as described capture important effects that should not be neglected in a high-fidelity full-envelope simulation. Of course, the physical math models in this implementation depend partly on calibration of semi-empirical constants determined by matching simulated flight characteristics with real observations. In all cases, any semi-empirical constants involved are constrained (bounded) to be physically representative of the effect being captured, i.e. the effect produced in simulation is physically plausible and consistent with observations.

IV. Propeller Slipstream Effects

A. Dynamic Pressure Effects

The effects of the propeller wake modify the forces and moments on the downstream surfaces vs what would result without slipstream effects. These forces and moments are determined through a component build-up approach that includes all surfaces immersed in the propeller slipstream. In each case, the local flow conditions are determined in part by a superposition of the wake flow and local relative flow given the local flow speed and angle. With this local flow speed and angle, the resulting forces and moments are determined by physical models that in part rely on lookup table data that is computed a priori. The approach described here will focus on a conventional configuration (single tractor-propeller aft-tail).

The most dominant effect of the propeller slipstream is the increased dynamic pressure on the downstream surfaces. This flow speed downstream is given by

$$V_{\text{downstream}} = V_{R,\text{local}} + k_w w \tag{21}$$

where k_w depends on the jet flow parameter m as given previously by Eq. 18 and has constants based on the proximity of the component to the propeller disc. Moreover, k_w is decayed depending on the local flow angle relative to the wake expansion angle, which itself is also formulated as a function of the jet flow parameter m. The local relative flow $V_{R,\text{local}}$ is determined from the kinematics of the component (freestream flow summed with flow components due to rigid-body rotations) and interference effects such as shielding of flow from one component on another, e.g., tail "blanketing."

Figure 6 shows the approach used in modeling this tail-surface shielding effect. The vertical fin for this aircraft operates in the flow shadow of the horizontal tail for off-nominal high angle conditions. A "flow shadow map" is constructed to model the fraction η_s relating the local relative flow to the total relative flow, that is

$$\eta_s = \frac{V_{R,\text{local}}}{V_{R,\text{total}}} \tag{22}$$

where $V_{R,\text{local}}$ is the flow exposed to the vertical fin, and $V_{R,\text{total}}$ is that determined from kinematics of the component. The fraction η_s ranges from zero (stagnant local flow) to 1 (no shielding present), and in this case for flow from below, η_s is functional defined here as

$$\eta_s = f(\overline{u}, \overline{v}) \tag{23}$$

where $\overline{u}$ and $\overline{v}$ are the direction cosines for the total relative flow vector. Figure 7 shows the flow shadow

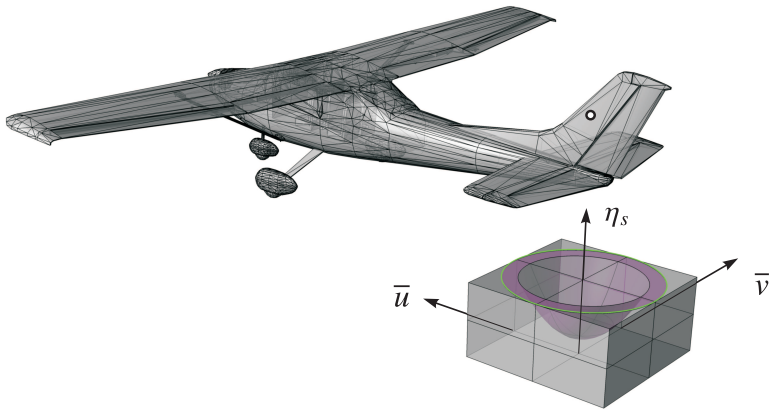

Figure 6. Flow shadow map approach used in modeling the shielding effect of the horizontal tail on the vertical fin for flow coming from beneath.

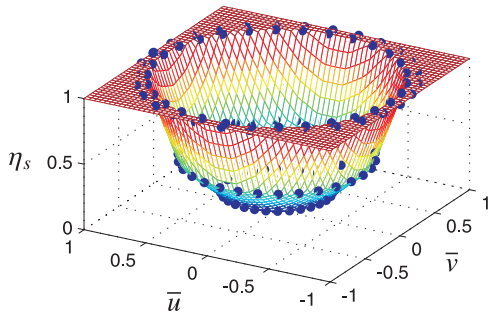

Figure 7. Flow shadow map data used in modeling the shielding effect of the horizontal tail on the vertical fin for flow coming from beneath for the Cessna 182 RC model.

map used to model this effect for the flow shadow on the vertical fin as a result of the horizontal tail beneath (case depicted in Fig. 6).

The flow shadow maps are used extensively to model shielding effects. For instance, flow shadow maps are also used on the horizontal tail surfaces when flow is from the opposite side of the surface (captures shielding from the vertical fin and fuselage). Moreover, flow shadow maps are used on the inboard sections of the wing for flow from either side at high sideslip. These maps in general are not axisymmetric, but instead sometimes squashed on one side depending on the local geometry that produces the shielding, or in some cases these flow shadow maps are 2D instead of 3D like Fig. 6. These maps are semi-empirical models that mimic the physics of the flow, but like many semi-empirical models (e.g., the myriad turbulence models with tunable parameters in CFD) these flow shadow maps that model the physics of the flow rely to some extent on tuning to produce results that mimic actual aircraft behaviors in high angle flight.

The use of flow shadow maps to decay the total flow due to shielding can have dramatic effects in a high propeller wash region. For instance, Fig. 8 shows the Oracle-sponsored biplane being flown by Sean Tucker in an aerobatic routine. This maneuver, called here a "knife edge slide," produces a flow shadow on the "leeward" side of the fuselage, which in this case is the right hand side. With airshow smoke on in this instance of a near quasi-steady maneuver, it is clear that the propeller wash jets along the leeward side of the fuselage unimpeded by the freestream flow approaching from the "windward" (left side). This effect is captured by the current flow shadow model combined with the propeller wash method. The flow shadow fraction η_s decays the oncoming total flow and by way of Eq. 21 the propeller wash remains. Thus, the right horizontal tail is almost completely immersed in the strong propeller wash (as the airshow smoke shows) while the left-hand-side horizontal tail experiences the sum of the propeller wash and total oncoming freestream. In the current approach, this effect is captured for all shieldable lifting surfaces at all attitudes

Figure 8. Sean Tucker performing a knife edge slide aerobatic maneuver with airshow smoke that shows strong propeller wash streaming along fuselage right side (aircraft bottom surface is to the camera).

by using for each component an independent flow shadow map as a function of the flow at the respective component.

B. Swirl Effects

For a right-handed propeller that spins clockwise when viewed from behind, a conventional vertical fin (above the axial centerline) will be exposed to swirl from the left side, that is, the flow coils clockwise down the fuselage when viewed from behind. The wash produces a left yaw in flight. (Note, this situation is reversed when flying inverted.) Swirl also impacts the wing root and horizontal tail with an upwash on the left side and a downwash on the right side. The wash produces a rolling moment to the right. Also, this swirl flow that coils around the fuselage produces an additional right rolling moment. All of these effects are included in the current propeller effects model. The swirl component itself is determined using PROPID. Taken together the right rolling moment produced by swirl flow counteracts the left rolling moment from the propeller reaction with the net positive right rolling moment. For a typical aerobatic RC/UAV configuration capable of hover, the net right rolling moment is near 40% of the propeller torque.

Modeling propeller swirl flow in normal cruise flight conditions is straightforward; however, for flight in off-nominal conditions, corrections must be applied. For non-axial flight – high angle of attack and/or high side slip – the misalignment of the swirl flow with the fuselage results in less right-airframe rolling torque, and consequently a higher net left rolling moment requiring greater aileron correction from the pilot. When in steep descent with a hover-capable airplane, the propeller wash is slowed by the oncoming reverse flow and eventually the propeller enters the recirculating vortex ring state (VRS). As this happens, the propeller torque can quickly dominate and produce a strong net left rolling moment, and this condition cannot be arrested by aileron input because for the most part the entire airframe is in reverse flow apart from the propeller in VRS.

C. Hover Damping

Another significant effect is "hover" damping, which is given that name here because the effect is dominant in hover, although it applies for all flight speeds. The effect has been included in the simulator FS One from the outset of its development,[12] and the basic effect is independently noted in Ref. 13

Figure 9 shows an airplane in a hover maneuver at three points in time. At time t, propeller wash is drawn at the disc, and this flow moves downstream in later time. Also in the figure, beginning at time t the aircraft motion begins – in the case drawn: edging to the right and yawing right. All the while the propeller slipstream continues on a straight line (ignoring any interaction between the propeller wash and airframe). The last instance shows that when the initial propeller wash finally impinges on the tail a sideslip angle is

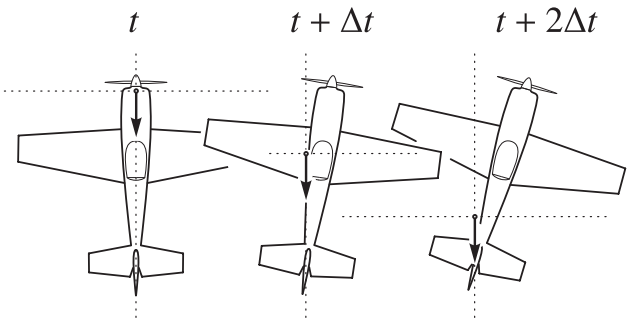

Figure 9. Physical explanation for yaw damping due to lagged propeller wash in near hover conditions.

produced on the vertical fin, and the resulting force produces both a side force and damping moment. The same effect occurs in pitch for the horizontal tail. In fact, any downstream component surface experiences this lagged damping effect that changes the local flow angle of attack and sideslip angle. Moreover, this effect happens at any flight speed with propeller wash, in which case the flow at the tail is the summation of the propeller wash and any other velocity components. In the case drawn for hover, this local flow angle correction is given by

$$\beta_{\text{hover damping}} = -\arctan\left(\frac{r\,l}{V_{\text{wash, lagged}}}\right) \tag{24}$$

where l is taken as the distance between the aircraft center of gravity and aerodynamic center of the lifting surface. In application these hover damping local flow angle corrections are "washed out" when the component surface falls outside of the propeller wake.

V. Simulation Framework

The propeller aerodynamics model described here is used in the full-envelope non-linear flight simulator FS One.[2,12] The simulation solves the full 6-DOF equations of motion using quaternions, and integration is carried out using a Runge-Kutta 4-th order scheme running at 300 Hz on a desktop PC. An efficient interpolation method is incorporated into the code to the extent that upward of 250 tables can be interpolated in realtime while running the simulation at 300 Hz and rendering the graphics through a typical PC gaming graphics card at ≈100 Hz or better. The simulator allows for pilot control input through a standard RC transmitter, from any standard USB joystick or from a data file.

VI. Results and Discussion – Simulations

In this section, flight simulations for the Funtana 90 shown in Fig. 10 are discussed. This aerobatic RC model is based on the Terzi T30 Katana full-scale aircraft. The maneuvers simulated are all aerobatic-type and demonstrate the strong propeller effects described. For each case, the flight is briefly described using the flight path trajectory and aircraft state data time histories. Superimposed on the trajectory is a skeleton outline of the aircraft oriented accordingly, and the ground trace is shown as a green line. Although the flight dynamics is carried out at 300 Hz, the time history data is plotted at a rate of 30 Hz, which is the recording rate used for these flights. For several of the flights described, the maneuver is complex and difficult to ascertain based on these short descriptions and graphics alone. In these cases, videos of these flights can be viewed online.[†] All of the flights presented here were performed by the author, and the results are consistent with observations (except that presented in Section VI.B as will be discussed). It is worth mentioning that the companion paper[2] includes maneuvers which also depend on propeller effects: knife edge flight, high-angle upright and inverted flight ("harriers"), rolling maneuvers at high angle ("rolling harriers") and an inverted spin of a biplane ("blender").

[†]All simulated flights were recorded as videos and are available online at `http://www.ae.illinois.edu/m-selig/animations`.

Figure 10. Funtana 90 used in simulations [rendering taken from simulator, wingspan of 1765 mm (69.5 in)].

A. Knife-Edge Power-On Spin

A wide range of aircraft spins can be performed by aerobatic airplanes, and some aircraft are more maneuverable than others. The particular Funtana 90 simulated here (Hangar 9 brand), can perform a knife-edge power-on spin which is on the "outer edges" of the extreme capability of most aerobatic airplanes; that is, most aircraft cannot be made to perform this maneuver. The maneuver is simulated here with the necessary control inputs and shown in Figs. 11 and 12.

The maneuver begins from a high-altitude push over to the downline and airspeed increases with advancing throttle. At ≈ 3 sec into the flight, down elevator and left aileron are fed into the controls simultaneously while the throttle input is reduced. Then, advancing throttle and rudder to their maximum limits are applied to bring the airplane into knife edge sideways flight (positive β). For a period of time thereafter, there is a complex exchange of angular momentum about the roll, pitch and yaw axes, but the maneuver final reaches quasi steady angular rates near 7.5 sec. While it might seem that more efficient use of controls could achieve this end more quickly, the pilot controls take only ≈ 4 sec to perform and in this process there are no wide excursions coinciding with the motion. Thus, the gyrations (bobbling) from 3 sec to 7.5 sec are caused by inherent system dynamics and not unsteady pilot control inputs. After 7.5 sec the spin rate is approximately 0.820 sec per cycle as seen in the trajectory (Fig. 11) where the interval between aircraft renderings is 0.205 sec, or once every 90 deg of spin rotation.

Once the steady spin develops, the ground trace (green line in Fig. 11) is nearly circular, and the changes in x and y time histories are thus sinusoidal (see Fig. 12). Termination of the spin begins at 15.8 sec where the control inputs are relaxed followed by up elevator to resume upright flight (positive pitch θ with bank angle ϕ closer to zero apart from that due to turning flight).

B. Upright Power-On Spin

The previous case developed into a steady knife edge spin with full controls, specifically full throttle, left rudder, down elevator and left aileron. Depending on the initial conditions, these same controls give rise to another type of spin – an upright power-on spin. Figures 13 and 14 show the flight. As described the same stick inputs are applied between 5 sec and 7.5 sec, and during this time the motion is approaching a quasi-steady upright spin (not a knife-edge spin as before).

Again the periodicity of the spin can also be seen in the trajectory (Fig. 13) where the interval between aircraft renderings is 0.125 sec, or once every 90 deg of spin rotation. In this case the flight is relatively short and the steady spin state is not reached. A near circular trace is nevertheless seen in Fig. 13 and also in the x and y time histories. The rotation (0.500 sec per cycle) in this upright case is faster than the knife-edge spin in part because the thrust pulls the center of gravity closer to the center of the spin axis. While this type of spin has been observed for aerobatic airplanes like this Funtana 90 model, this particular spin condition was not attempted or observed in flight tests, and thus this spin state cannot yet be validated for this aircraft.

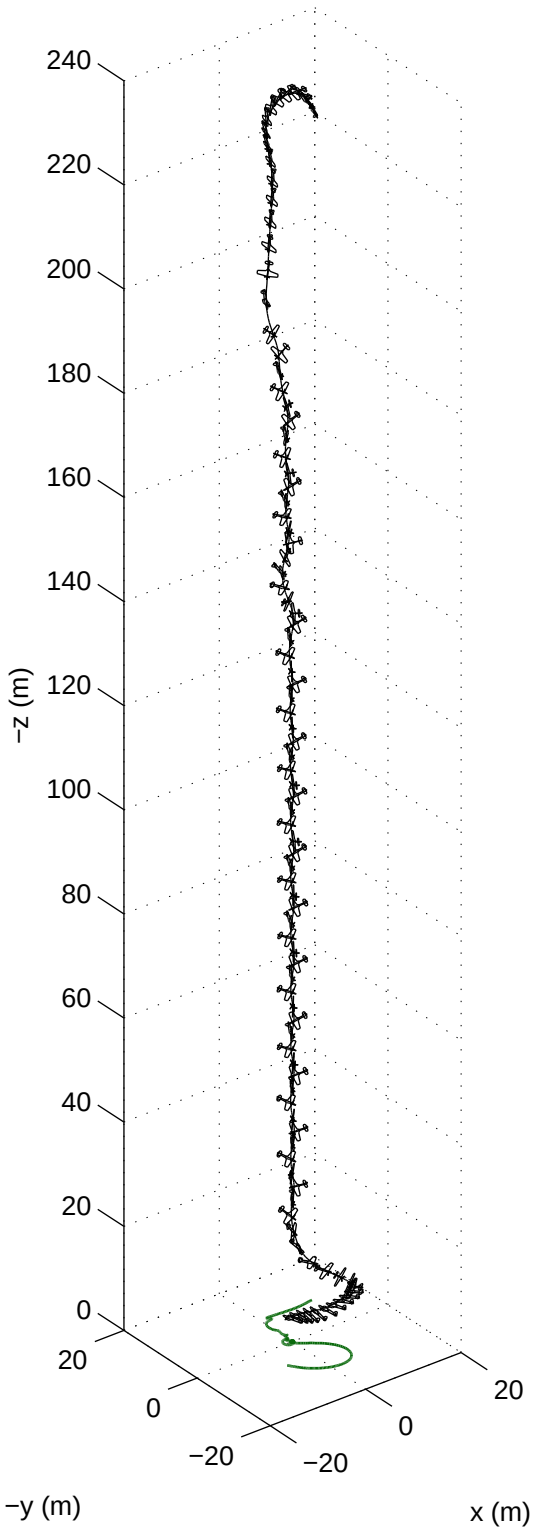

Figure 11. Trajectory of the Funtana 90 aerobatic aircraft performing knife-edge power-on spin [aircraft magnified 2 times normal size and drawn every 0.205 sec, wingspan of 1765 mm (69.5 in)].

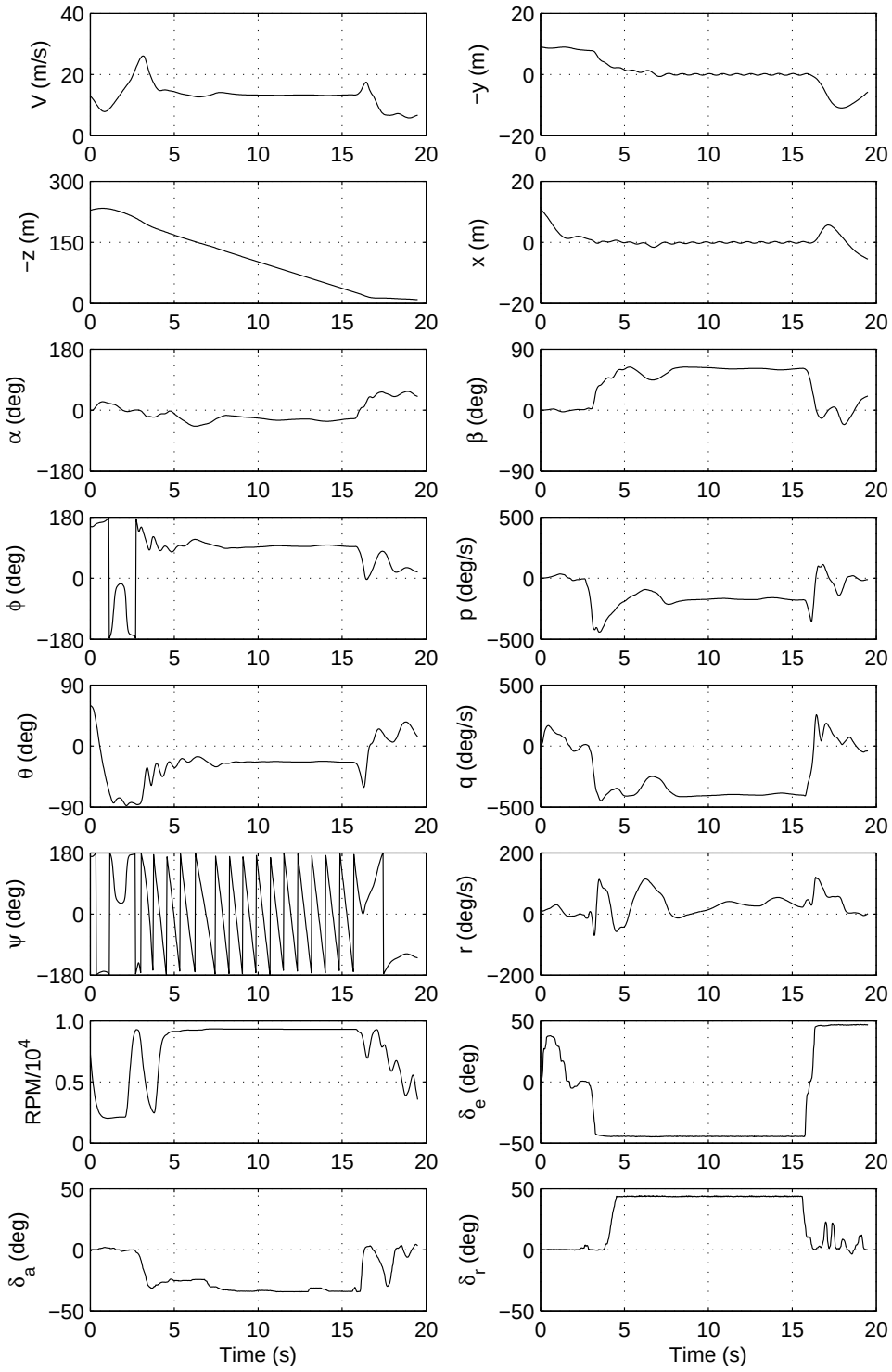

Figure 12. Time history the Funtana 90 aerobatic aircraft performing knife-edge power-on spin (see Fig. 11 for trajectory).

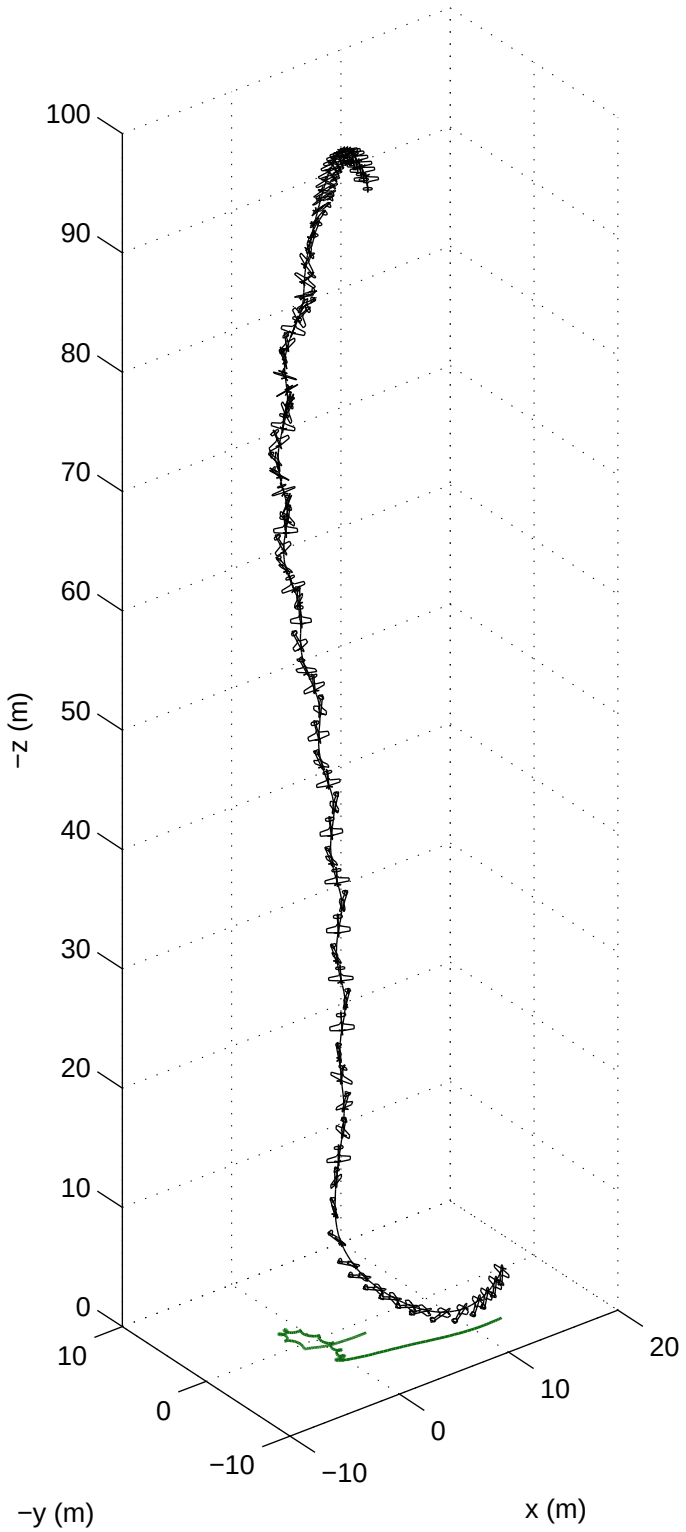

Figure 13. Trajectory of the Funtana 90 aerobatic aircraft performing an upright power-on spin [aircraft normal size and drawn every 0.125 sec, wingspan of 1765 mm (69.5 in)].

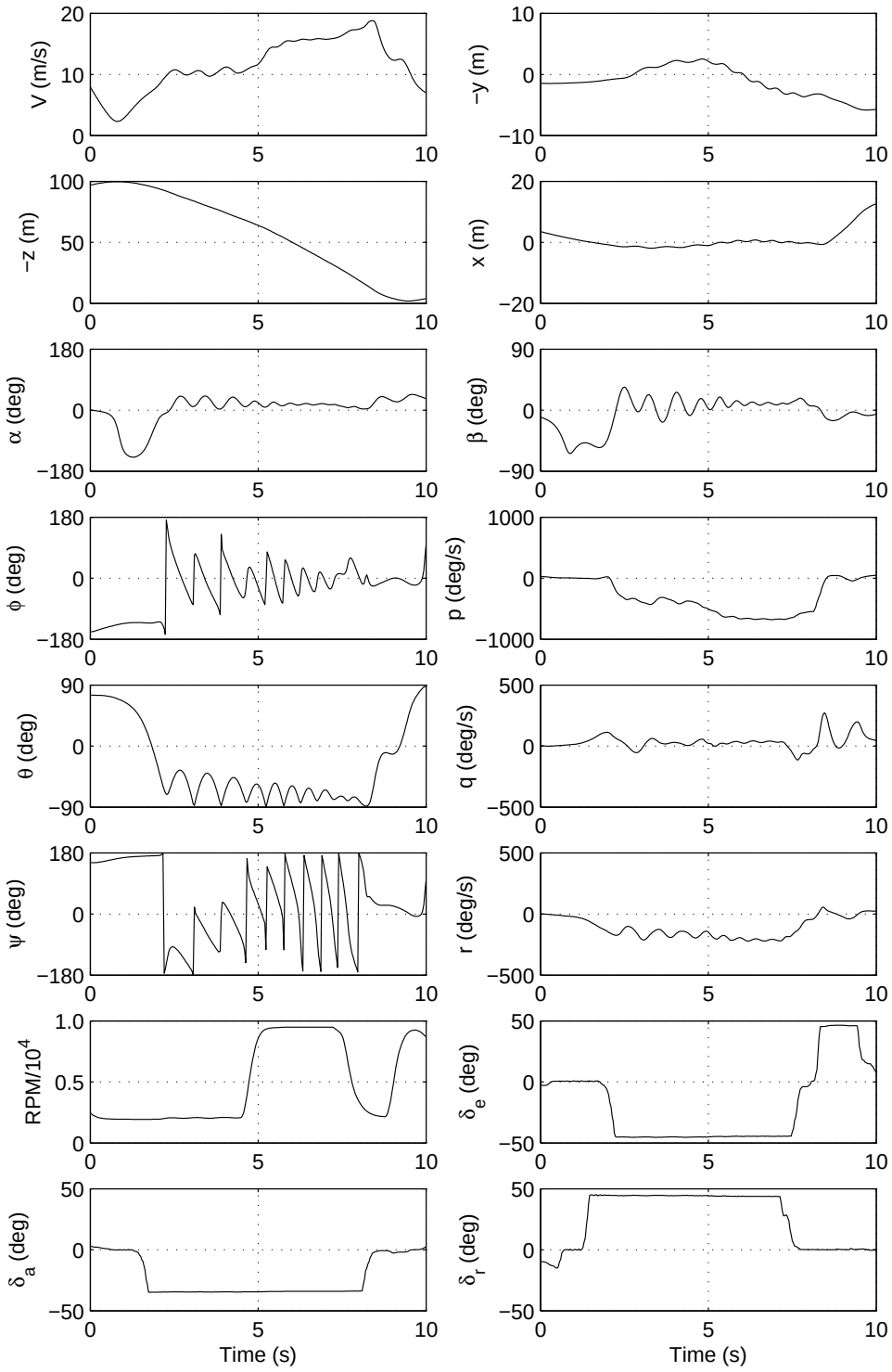

Figure 14. Time history the Funtana 90 aerobatic aircraft performing an upright power-on spin (see Fig. 13 for trajectory).

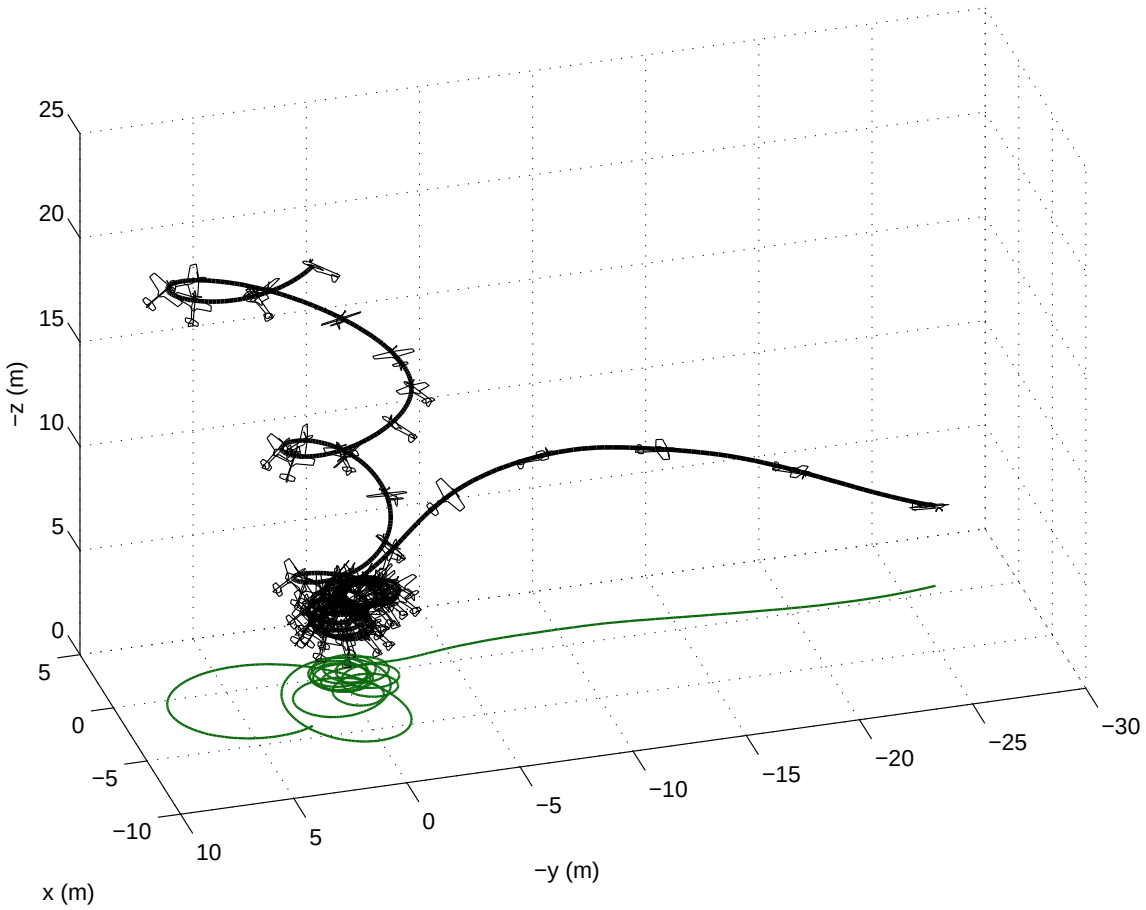

Figure 15. Trajectory of the Funtana 90 aerobatic aircraft performing an inverted pirouette [aircraft normal size and drawn every 0.5 sec, wingspan of 1765 mm (69.5 in)].

C. Inverted Power-On Pirouette

As described in the companion paper,[2] airplanes like the Funtana 90 can fly inverted at high angle of attack (the so-called inverted harrier). In this condition, the aircraft can be banked to turn and with enough control input the turn can be tightened. Figures 15 and 16 show this happening for the Funtana 90. While the condition is entered from some elevation ($z = -20$ m high), the throttle is reduced to initially descend and then increased again to maintain near constant elevation above the ground (z). At this point the airplane pirouettes with a radius of curvature of approximately 1.2 m at a rate of 2.24 sec per cycle. In the final steady pirouette, the angle of attack is ≈ 80 deg with a sideslip of ≈ 30 deg. The aircraft is largely flying on thrust from the propeller with only a slight amount of lift from the lifting surfaces, which at this point mainly serve as control effectors. Finally, it is interesting to note that the control inputs to achieve this steady-state pirouette are *identical* to the prior knife edge spin and upright spin conditions.

Its worth mentioning that reversing the lateral controls (rudder and aileron) will reverse the direction of the spins in these three cases only if the propeller spin direction is also changed. In other words, these spins take advantage of and depend on gyroscopic forces, P-factor and swirl effects which are propeller spin-direction dependent as governed by the sign of Ω.

D. Hovering Sequence

The high thrust-to-weight ratio capability of modern small UAVs makes possible hovering flight, and this type of flying has become quite popular in model aviation. With the large control surfaces immersed in propeller

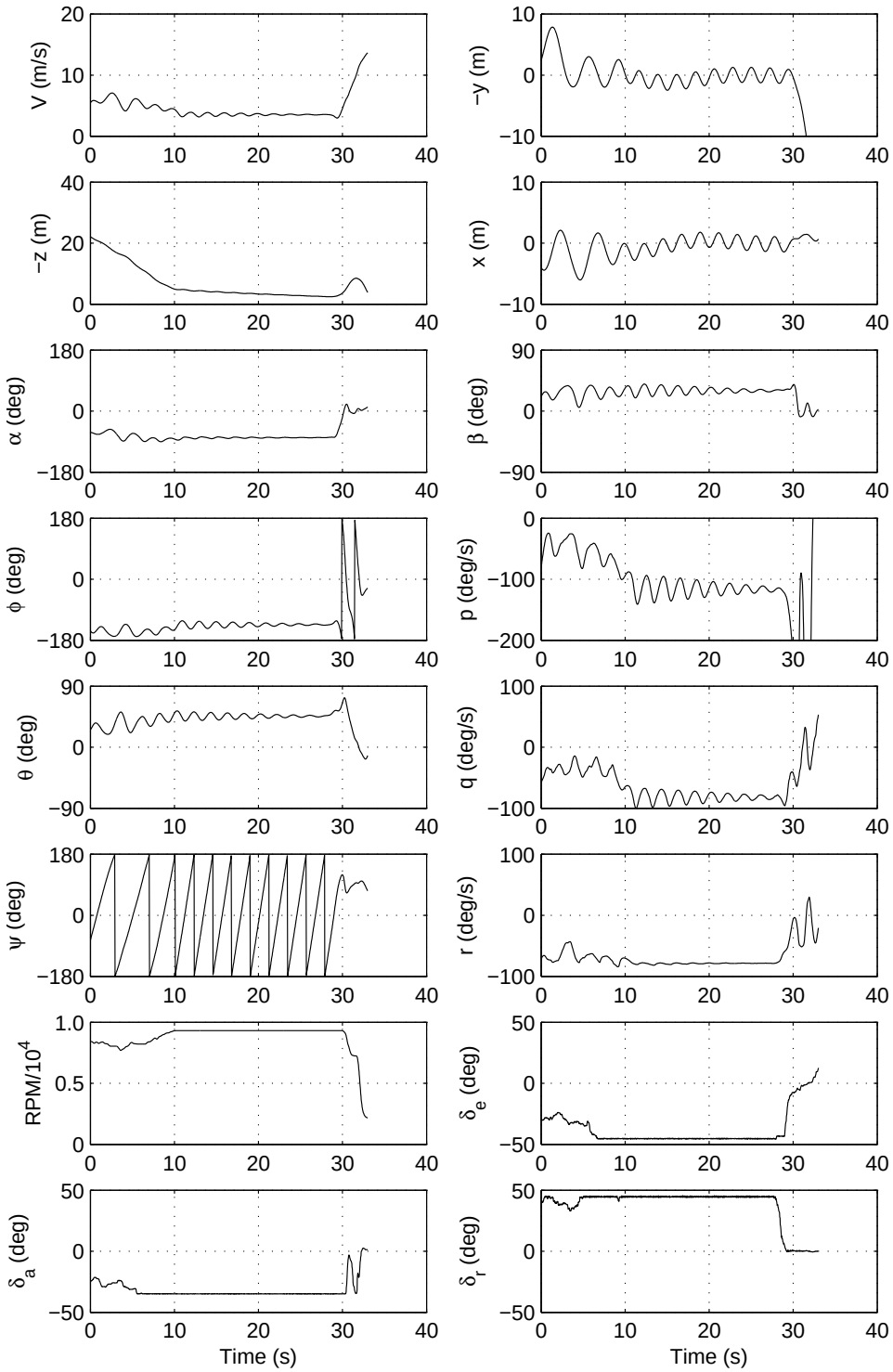

Figure 16. Time history the Funtana 90 aerobatic aircraft performing an inverted pirouette (see Fig. 15 for trajectory).

wash, the Funtana 90 RC-model configuration with a thrust-to-weight ratio of 2:1 is highly maneuverable in hover.

To start, it is useful to contrast pilot techniques in cruise flight vs hovering flight, which is relatively

new and being advanced by high-performance RC models. In normal cruise flight, as noted in Ref. 6, the elevator and rudder are displacement controls used to set a trim position. The ailerons, however, are a rate control used to set the roll rate. In hovering flight, however, the elevator, rudder and ailerons all become rate controls. Moreover, in hover, the aircraft is never in vertical trim; it is always unstable, tending to move off of perfect vertical alignment. Thus, the two modes of flight (cruise vs hover) are quite different, and it requires a change in piloting strategy (mental thinking and control inputs) when switching between the two. Another, observation involving pilot strategy is that pilots in hover regularly pulse the throttle command. This technique allows a pilot to continuously gauge the control power (maneuver power) of the airplane and thus anticipate and maneuver through any dynamic response. Of course, while these modes of flight are distinctly different, flying back and forth between these two regimes becomes second nature for experienced pilots.

As shown in Fig. 17, the trajectory plot is cluttered because of the near stationary flight for certain periods in the sequence. There are three main hovering stages that make up this full hovering sequence. For the entire time history shown in Fig. 18, the airplane pitch is ≈ 90 deg – pointed straight up. Also, for the entire sequence, small inputs on elevator and rudder are used to maintain the 90-deg hovering attitude and maintain a sense of pitch and yaw control power at any given point in time.

In the first stage from 2.7 to 13.4 sec, the control strategy was to maintain the aircraft orientation as 'top-side' to the pilot, i.e. near zero roll rate (p) while keeping the aircraft in top-view position from the perspective of the pilot. In this position, without any aileron input, the aircraft will roll left due to propeller torque and the counteracting, but smaller, aerodynamic torques from downstream surfaces. Thus, to maintain the orientation, right aileron pulses are used continuously to zero the net rolling moment. As described, these inputs are also pulsed (see spikes in δ_a) to maintain a constant sense of control power. During this period of time, the x-y position changes little because the aircraft is in hover.

The second stage of hover begins when the airplane reaches the position $-y = -2.5$ m (see side view in Fig. 17). During this time, which begins around 20 sec, no aileron input (δ_a) is applied, and the airplane enters a slow torque roll at a rate of $p \approx -100$ deg/sec. Only rudder and elevator deflections are applied to maintain the 90-deg vertical pitch.

Finally, for the third stage, the airplane moves to the position $-y = -10$ m (see side view in Fig. 17) and is allowed to climb to a height of 6.7 m. At this point, the airplane is allow to descend vertically and enter the propeller vortex ring state. When this happens, hovering in this regime is difficult for the pilot, and the control inputs are excited by the pilot while managing the rapid increase in roll rate. This descent through the vortex ring state happens three times ending at 50 sec, and each time the roll rate increases after starting from near zero.

E. Power-Effects Sequence

In this last sequence (Figs. 19 and 20), a number power-effects maneuvers are presented. These effects and others will be described. For the first few seconds,[‡] the airplane moves as the propeller is 'started' and the control surfaces are 'wiggles,' which are ritual acts for a pilot. As the airplane rests on the ground the angle of attack and side slip are ill-defined as seen by the 'chatter' in the initial and final data in their time histories.

After takeoff the airplane is rolled inverted with cross-controls on aileron and rudder ($t = 6.4$ sec). At 10 sec, a burst of throttle and down elevator are used to rapidly pitch the aircraft vertical (see Fig. 19), followed by a 180-deg roll at 12.6 sec. As the airplane climbs, the throttle is reduced and the airspeed slows to near zero. At this point in the climb where z peaks (17.2 sec), a burst of throttle and down elevator are used to pitch the airplane straight down rather than entering a tail slide condition. At the bottom of the downline at 19.5 sec, elevator and throttle are again used to rapidly pitch the airplane. These rapid pitch maneuvers (also seen in q and θ) are a result of strong propeller wash effects impinging on the horizontal tail with appropriate surface deflections.

[‡]In the simulation at $t = 0$ sec the airplane is placed on the ground which includes random elevation perturbations to simulate bumpy ground. The airplane thus rocks in roll (p) when the sequence begins. At 1 sec, throttle is pulsed to 'start' the engine and the propeller accelerates, which produces another small wing rock (p). At 3.2 sec, the control surfaces (sticks) are wiggled, and again the wing rocks – this time due to the inertia of the aileron motions and tail wag from tail wheel motion tied to the rudder.

The next significant propeller-effects maneuver begins after climbing to the position near $x = -30$ m (30 sec). At this point, full throttle, full right rudder, full down elevator and some left aileron are used to enter a near-zero-pitch inverted turning descent. At this point if throttle were reduced the aircraft would enter a flat spin, but with continued full throttle to show propeller effects the airplane pitches over (near 42 sec) and is flown to a landing (see Fig. 19) at the pilot position.

VII. Conclusions

As described in this paper, traditional propeller effects and new effects from strong propeller wash are important in simulating flight dynamics over the full ±180 deg high-angle full-envelope flight considered here. These propeller effects include not only the traditionally considered thrust, torque and normal force but also important slipstream and momentum effects that dominate in low-speed to hovering conditions. In particular, there are several damping forces and moments that affect the handling qualities in and around slow-speed and hovering flight. Piloted flight simulation results for a small RC/UAV configuration demonstrate that these important effects drive the flight dynamics in a number of maneuvers, which was shown here with knife-edge power-on spins, upright power-on spins, inverted power-on pirouettes, hovering maneuvers, and rapid pitch maneuvers that were all assisted by strong propeller-force and propeller-wash effects. The overall approach that factors in many considerations is made viable by incorporating this propeller model in a larger aerodynamics component-based simulation framework that is discussed in a companion paper.

Acknowledgments

The author would like to thank Brian W. Fuesz and Chris A. Lyon for programming the framework of the simulator that includes the methods described in this paper. Also, the aircraft design and development group at Horizon Hobby is gratefully acknowledged for partly supporting the initial development of the simulator. The author wishes to acknowledge Pritam P. Sukumar for his efforts in assisting in preparation of some of the plots included in this paper.

References

[1]McCormick, B. W., *Aerodynamics, Aeronautics, and Flight Mechanics*, John Wiley & Sons, New York, 2nd ed., 1995.

[2]Selig, M. S., "Modeling Full-Envelope Aerodynamics of Small UAVs in Realtime," AIAA Paper 2010–7635, August 2010.

[3]Hibbs, B. and Radkey, R. L., "Calculating Rotor Performance with the Revised PROP Computer Code," Tech. rep., Wind Energy Research Center, Rockwell International, Golden, CO, RFP-3508, UC-60, 1983.

[4]Selig, M. S. and Tangler, J. L., "Development and Application of a Multipoint Inverse Design Method for Horizontal Axis Wind Turbines," *Wind Engineering*, Vol. 19, No. 5, 1995, pp. 91–105.

[5]Selig, M. S., "PROPID - Software for Horizontal-Axis Wind Turbine Design and Analysis," `http://www.ae.illinois.edu/m-selig/propid.html`, 1995–.

[6]Etkin, B. and Reid, L. D., *Dynamics of Flight – Stability and Control*, John Wiley & Sons, New York, 2nd ed., 1995.

[7]Guerrero, I., Londenberg, K., Gelhausen, P., and Myklebust, A., "A Powered Lift Aerodynamic Analysis for the Design of Ducted Fan UAVs," AIAA Paper 2003–6567, September 2003.

[8]Abramovich, G. N., *The Theory of Turbulent Jets*, The MIT Press, Cambridge, MA, 1963.

[9]Schetz, J. A., *Injection and Mixing in Turbulent Flow), series = AIAA Progress in Astronautics and Aeronautics, publisher = AIAA, Reston, VA, year = 1980,.*

[10]Kuhn, R. E., Margason, R. J., and Curtis, P., *Jet Induced Effects: The Aerodynamics of Jet and Fan Powered V/STOL Aircraft in Hover and Transition*, AIAA Progress in Astronautics and Aeronautics, AIAA, Reston, VA, 2006.

[11]Veldhuis, L. L. M., *Propeller Wind Aerodynamic Interference*, Ph.D. thesis, Department of Aerospace Engineering, Delft University of Technology, The Netherlands, 2005.

[12]"FS One, Precision RC Flight Simulator," Software Developed by InertiaSoft, Distributed by Horizon Hobby, Champaign, IL, 2006.

[13]Frank, A., McGrew, J. S., Valenti, M., Levine, D., and How, J. P., "Hover, Transition, and Level Flight Control Design for a Single-Propeller Indoor Airplane," AIAA Paper 2007–6318, August 2007.

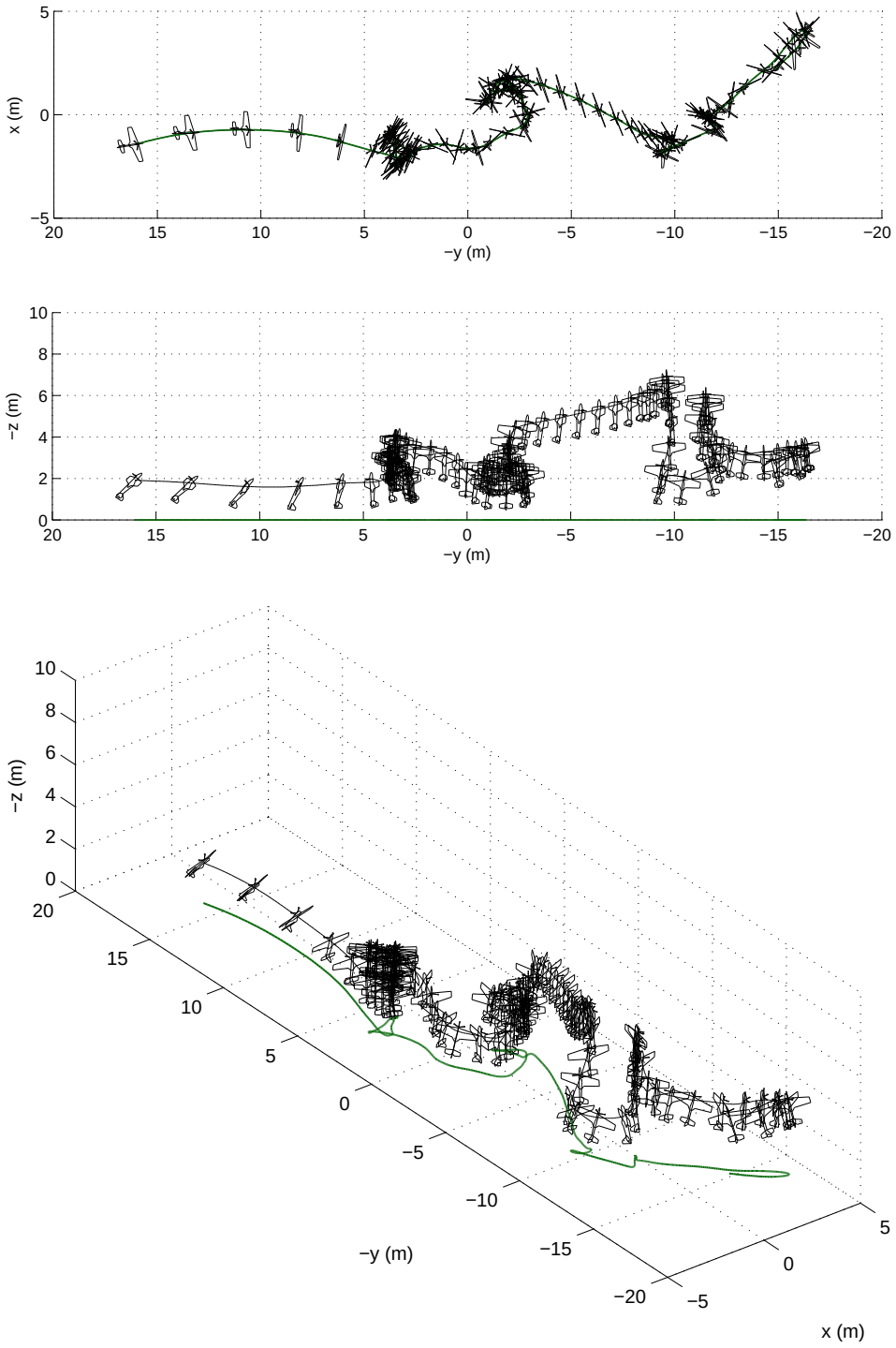

Figure 17. Trajectory of the Funtana 90 aerobatic aircraft hovering [aircraft normal size and drawn every 0.5 sec, wingspan of 1765 mm (69.5 in)].

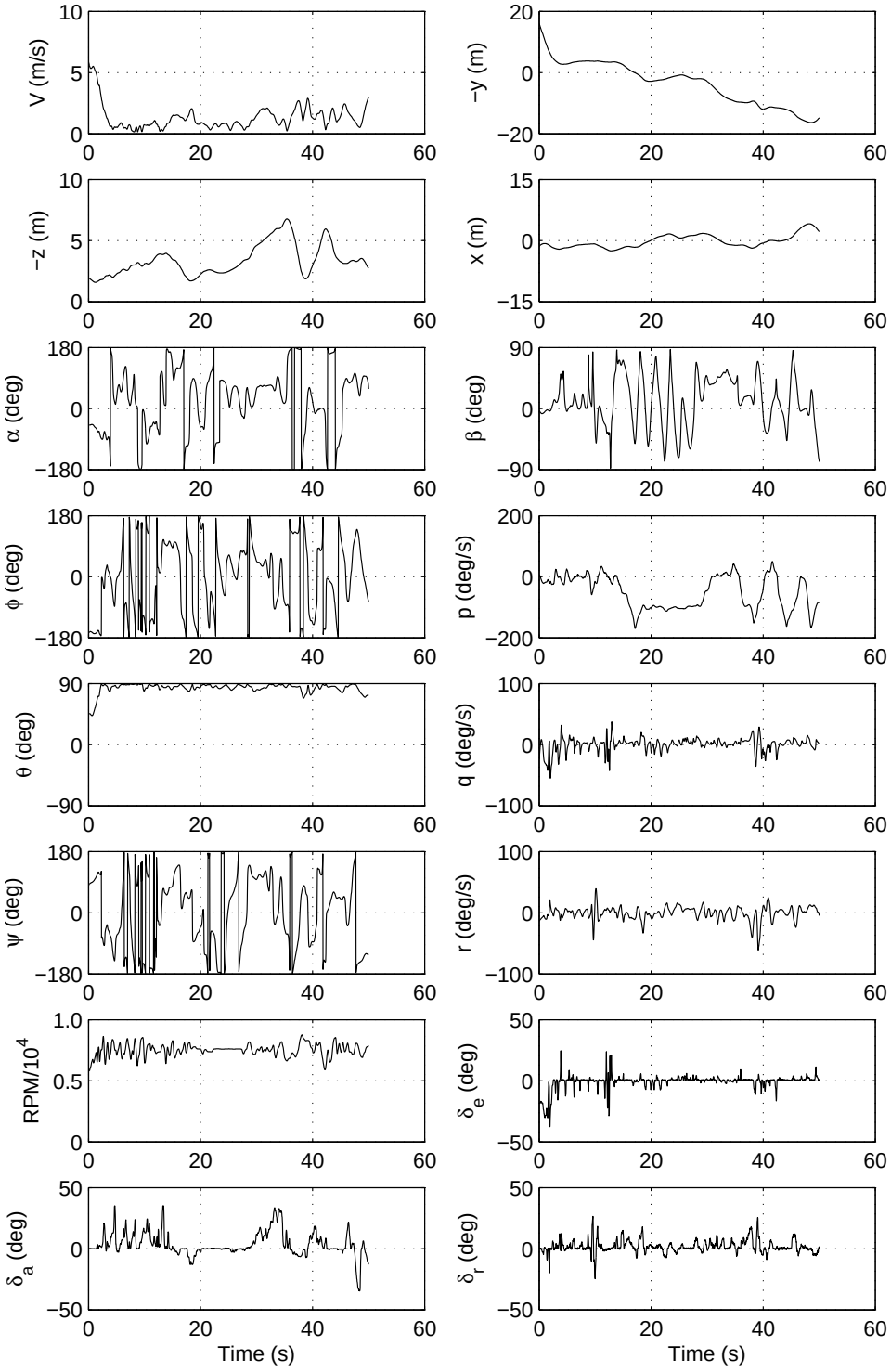

Figure 18. Time history the Funtana 90 aerobatic aircraft hovering (see Fig. 17 for trajectory).

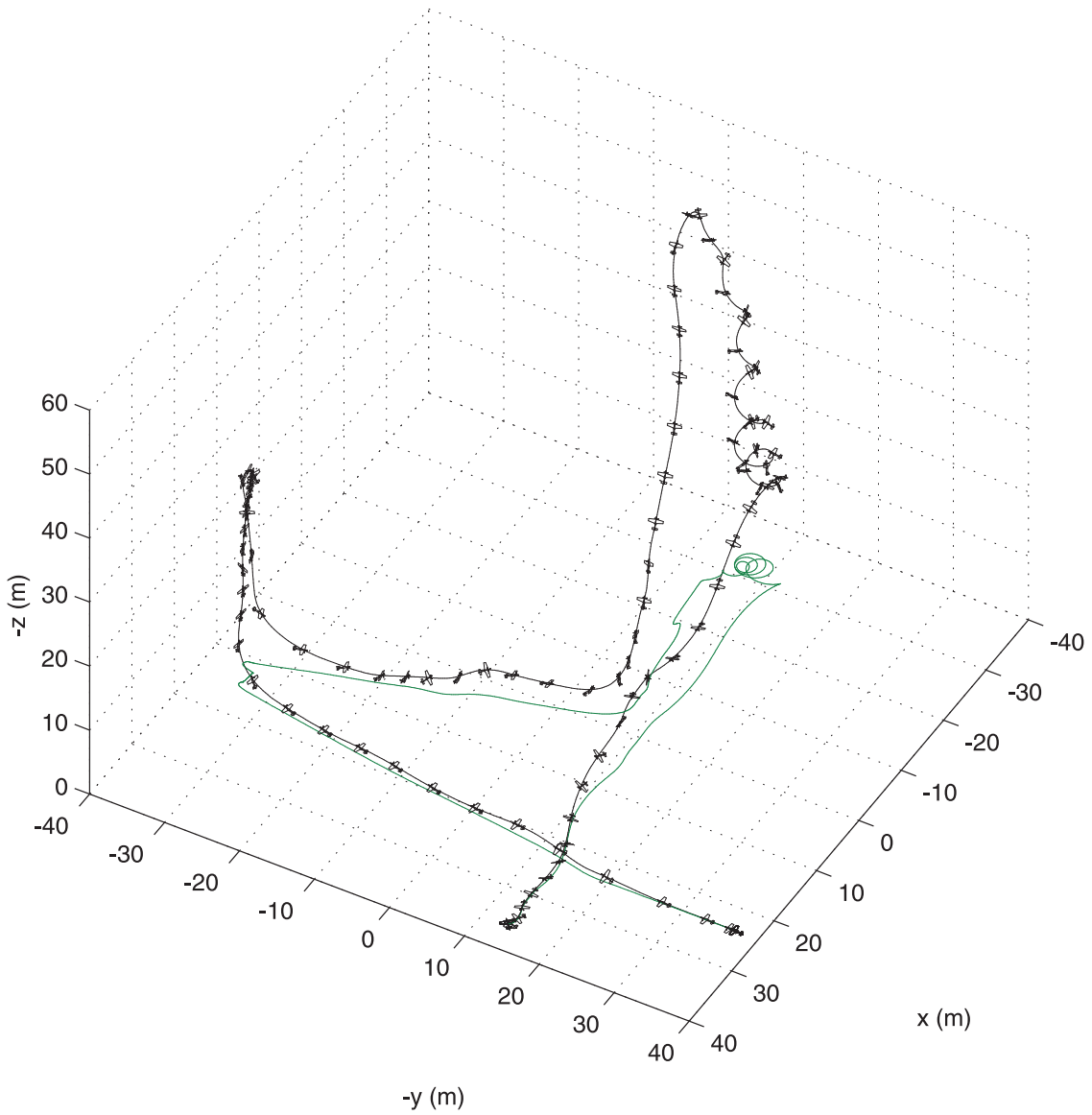

Figure 19. Trajectory of the Funtana 90 aerobatic aircraft performing an aerobatic sequence with power effects [aircraft normal size and drawn every 0.5 sec, wingspan of 1765 mm (69.5 in)].

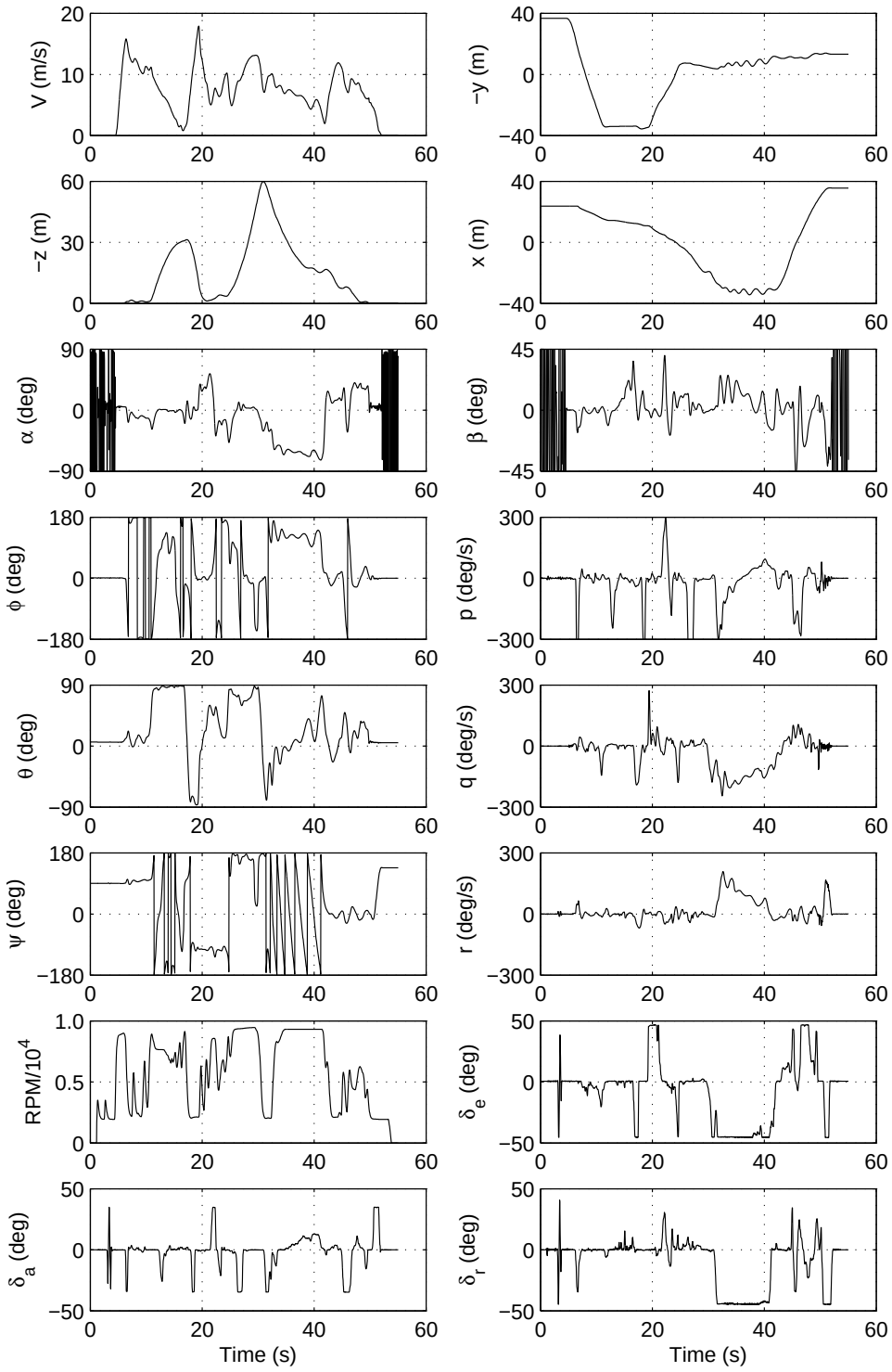

Figure 20. Time history the Funtana 90 aerobatic aircraft performing an aerobatic sequence with power effects (see Fig. 19 for trajectory).